CrystEngComm

Accepted Manuscript

ROYAL SOCIETY OF CHEMISTRY

www.rsc.org/crystengcomm

In situ total X-ray scattering study of the formation mechanism and structural defects in anatase TiO_2 nanoparticles under hydrothermal conditions†

Jian-Li Mi,[a] Kirsten M. Ø. Jensen,[b] Christoffer Tyrsted,[c] Martin Bremholm[c] and Bo B. Iversen*[c]

[a]*Institute for Advanced Materials, School of Materials Science and Engineering, Jiangsu University, Zhenjiang 212013, China*

[b]*Applied Mathematics and Applied Physics, Columbia University, New York, USA*

[c]*Center for Materials Crystallography, Department of Chemistry and iNANO, Aarhus University, DK-8000 Aarhus C, Denmark. E-mail*: bo@chem.au.dk

† Electronic Supplementary Information (ESI) available: Time evolution of *in situ* PXRD patterns; details and examples of the refinements of the PDFs of the ordered structure, the oxygen vacancy model, and OH defect model; details of the Rietveld refinement of the PXRD data; the oxygen *z* coordinate and the closest Ti-O distance as functions of reaction time; determination of the crystallinity of TiO_2 nanoparticles by PXRD.

Abstract: Polymorphism, morphology, particle size, and defects play key roles in the physical and chemical properties of nanoparticles. In hydrothermal synthesis of metal oxide nanoparticles, it is important to understand the influence of the specific precursor on these characteristics. Here, the formation mechanism of anatase TiO_2 nanoparticles by hydrolysis of titanium isopropoxide under hydrothermal conditions is studied by *in situ* total X-ray scattering and pair distribution function (PDF) analysis. It is shown that the amorphous precursor structure has short-range order up to ~6.5 Å consisting of titanium hydroxide clusters made from TiO_6/TiO_5 units in an arrangement related to anatase. Insight into the structural disorder of the anatase TiO_2 nanocrystals is obtained from both PDF and powder X-ray diffraction (PXRD) analysis. Defects of OH species

are present on the surface of the nanocrystals, and their concentration correlates strongly with the particle size. Even though the formation of anatase TiO_2 under hydrothermal conditions resembles a solid-state phase transition from amorphous titania, the crystallization and grain growth kinetics of the nanocrystals are different due to the effects of the solvent.

Introduction

TiO_2 is one of the most important and widely used metal oxides because it is a low-cost, nontoxic and chemically inert material with a range of very attractive applications such as photocatalysis, hydrogen production and photovoltaic cells.[1-4] It is well established that the properties of TiO_2 nanoparticles are highly dependent on the structural polymorph, particle size, crystal structure, morphology, crystallinity, defects and structural disorder.[5-6] In nature TiO_2 is found in three crystalline polymorphs: rutile, anatase, and brookite, all of which consist of TiO_6 octahedra that share either edges or corners. Rutile is the thermodynamically stable phase at ambient conditions, while anatase is found to be the stable phase on the nanoscale due to surface effects.

Hydrothermal synthesis is a facile way to produce metal oxide nanomaterials. When different precursors are used for hydrothermal synthesis, it is often observed that the product has specific characteristics, e.g. polymorphs, morphologies, particle sizes and defects, which all strongly affect the material properties. However, the processes occurring during the formation of nanoparticles are not well understood, and this to a large extent prevents rational synthesis of new materials. Investigation of nanocrystal formation processes is highly challenging because it is difficult to obtain atomic scale information for very small particles or aggregates during the reaction.[7] This is known as "nanostructure problem".[8] To open the "black" box of hydrothermal synthesis, *in situ* synchrotron powder X-ray diffraction (PXRD) has been used to study nanocrystal growth of a wide range of nanoparticles.[9-13] In particular a few studies have been devoted to the study of TiO_2 crystallization and growth by *in situ* synchrotron PXRD under solvothermal, hydrothermal or sol-gel conditions.[14-18] However, PXRD analysis

only applies to crystalline materials. A deeper understanding can be achieved if atomic scale information can be assessed in the amorphous state before crystallization. This is possible by measuring total X-ray scattering from the sample and calculating the atomic pair distribution function (PDF).[19-24] Because PDF analysis makes use of both Bragg and diffuse scattering intensities, it allows extraction of structural information from liquids, glasses, amorphous materials, nanocrystalline and disordered materials as well as crystalline structures. Total X-ray scattering is thus a well suited technique for *in situ* studies of chemical reactions, but it is challenged by the signal to noise ratio obtainable from dilute suspensions when data are collected with second time resolution. Nevertheless, total X-ray scattering studies have provided information on both atomic and microstructural changes taking place during hydrothermal processes all the way from the amorphous precursor to the nanocrystalline product.[25-29] In the literature, several studies have focused on understanding the atomic structure of solid amorphous TiO_2 by PDF analysis.[30, 31] However, little is known about the formation and growth mechanisms from the amorphous precursor to the crystalline TiO_2 nanoparticles during the hydrothermal process.

In addition to knowledge about the hydrothermal synthesis processes, it is essential to understand the defects and disorder in the nanoparticle structure. Although significant progress has been made with e.g. scanning tunneling microscopy (STM) for studying the surface defects of rutile TiO_2 (110) surfaces,[32] it remains highly challenging to obtain direct experimental evidence about the surface and bulk defects in nanoparticles particularly during dynamic formation processes. By extracting the occupancies of Ti and O atoms, Rietveld refinement of PXRD data has been used to study possible defects in TiO_2 nanoparticles.[33] However, PXRD analysis assumes long range order, which is not present in very small nanoparticles. Therefore, the apparent oxygen deficiency observed by PXRD may be an artifact due to model inadequacy. Recently, electron paramagnetic resonance has also been applied to study the defect centers for metal oxides such as ZnO.[34,35] Here, we show that PDF analysis is a straightforward and direct method that allows the determination of both short-range and long-range structures of nanoparticles of any size. We furthermore discuss the different,

but complementary, structural information about the oxygen occupancy obtained by PDF and PXRD.

Results and discussion

Nanostructure

The initial mixing of water with the titanium isopropoxide solution produces a homogeneous suspension of white titanium hydroxide. Time resolved PDFs of the transformation from this aqueous precursor suspension to anatase TiO_2 nanocrystals under hydrothermal conditions are shown in **Fig. 1a**. It is clear that only short-range order to approximately 6.5 Å is present in the precursor. At the beginning of the synthesis, there is no apparent change on the PDF patterns for the precursor, but after a very short induction period for crystallization (about 3 seconds), anatase TiO_2 nanoparticles are formed as longer range order is observed. Thus, the formation of anatase TiO_2 under hydrothermal synthesis is likely via a solid state phase transition from amorphous titania. This is also supported by the time evolution of the PXRD patterns with a time resolution of 1 s (**Fig. S1**). The intensity of the amorphous "peak" at $2\theta = 2.6°$ of the PXRD pattern is constant before crystalline TiO_2 appears suggesting the amorphous precursor is not dissolved during the induction stage. Once the crystallization commences, the intensity of the anatase peaks increases while the intensity of the amorphous "peak" decreases. Thus, it is unlikely that the crystallization follows a dissolution-precipitation mechanism, and the formation of anatase TiO_2 under hydrothermal synthesis resembles that of a direct solid-state phase transition from amorphous titania. **Fig. 1b** shows a comparison of the PDF patterns before the onset of heating (t = 0 s) and after a reaction time of 3, 9, 15 s as well as the final product obtained after 20 min. Clearly, there is a close relationship and smooth progression of the coordination in the precursor to the crystalline TiO_2. The intensity of the shortest Ti-O shell (1.97 Å in anatase) increases as the crystallization progresses indicating the Ti-O coordination number increases during the crystallization of the nanoparticles. The local order of the precursor is quite closely related to that of anatase TiO_2. The

characteristics of the local order of the amorphous precursor may have critical influence on the formation of TiO_2 products with anatase structure.

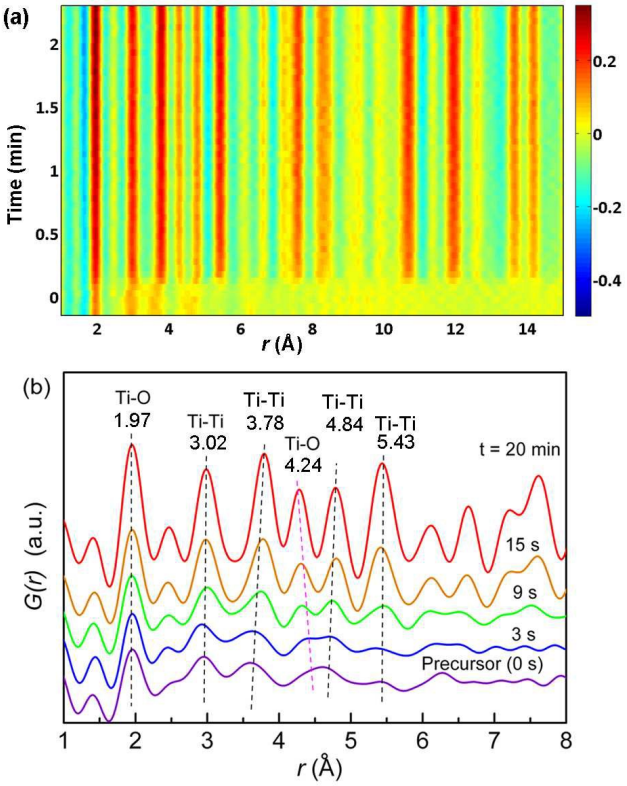

Fig. 1 (a) Time resolved *in situ* PDFs at a reaction temperature of 250 °C showing the hydrothermal transformation of the amorphous precursor with only short-range order to nanocrystals with long-range order. (b) PDF patterns at reaction times of 0, 3, 9, 15 s, and 20 min, respectively. The values of the representative interatomic distances are from an anatase TiO_2 structure with a unit cell of a = 3.779 Å and c = 9.451 Å.

Before analyzing the structure of the precursor, the PDF data of the crystalline TiO_2 particles are modeled and then refined using the anatase structure. **Fig. 2** shows the refined PDF patterns for the data collected after 20 min of reaction. By including the whole r range data (1.5 Å < r < 60 Å) in the real space PDF refinement, the structural information listed in **Table 1** is obtained. The unit cell parameters of anatase TiO_2 after 20 min are a = 3.779(1) Å and c = 9.451(5) Å, and the nanocrystals have an average particle size of 5.4(3) nm. The representative interatomic distances are marked in the anatase structure as shown in **Fig. 2**. The PDF peaks of the crystalline TiO_2 (t = 20 min)

corresponding to the interatomic distances are also marked in **Fig. 1b**.

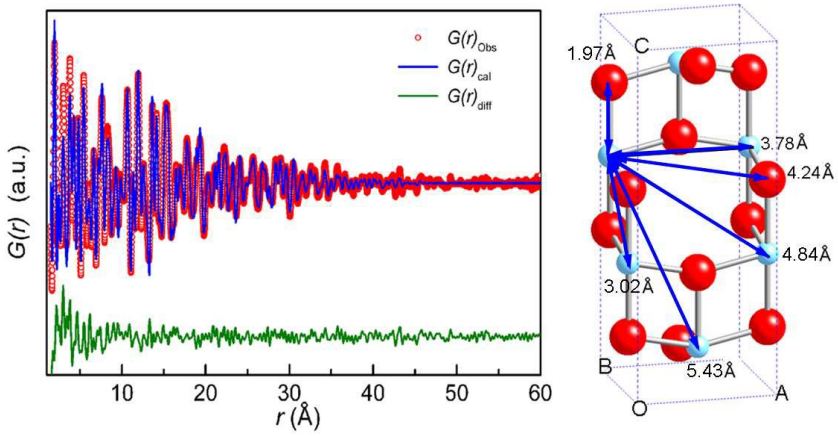

Fig. 2 Fit to the PDF *G(r)* collected after 20 min reaction time with anatase TiO_2 structure.

Table 1 Refinement residuals and selected parameters for the different models describing the PDF data obtained after 20 minutes reaction.

Structure model	Ordered structure		Oxygen vacancy		OH defects
Data range (Å)	1.5-60	1.5-7	1.5-60	1.5-7	1.5-7
Data points	5851	551	5851	551	551
Refined parameters	8	5	9	6	9
R_{WP} (%)	25.2	31.1	25.7	27.2	24.8
Scale factor	0.053(2)	0.055(3)	0.053(2)	0.056(5)	0.071(1)
a (Å)	3.779(1)	3.779(4)	3.778(1)	3.779(5)	3.777(7)
c (Å)	9.451(5)	9.451(9)	9.451(5)	9.455(1)	9.483(2)
U (Ti) (Å^2)	0.0058(5)	0.0059(9)	0.0079(8)	0.0066(8)	0.0058(9)
U (O) (Å^2)	0.015(1)	0.015(2)	0.011(2)	0.0099(3)	0.014(2)
Oxygen (occ)	100%[a]	100%[a]	82.4(5)%	72.7(6)%	100%[a]
Particle size (nm)	5.4(3)	5.4[a]	5.7(3)	5.7[a]	5.4[a]

[a]These parameters were fixed during the refinement.

The known crystal structure of anatase TiO_2 is used to construct models to analyze the local structure of the precursor. As shown in **Fig. 1b**, the primary difference between the local order of the precursor and anatase TiO_2 is that the Ti-O shell at 4.24 Å in anatase TiO_2 is not evident in the precursor. However, the characteristics of the Ti-Ti shells at 3.02, 3.78, 4.84 and 5.43 Å in anatase TiO_2 are clearly present in the precursor. Thus, the Ti atoms are placed in a structure that is closely related to anatase structure, while the local structure of the oxygen atoms differ from anatase. The Ti-Ti shells at 3.02 and 5.43 Å remain largely unchanged throughout the transformation, while the Ti-Ti shells at 3.78 and 4.84 Å are significantly shorter in the precursor. This indicates more dense atomic packing along the *a*- and *b*-axis directions in the precursor (see **Fig. 2**), while the third dimension along the *c*-axis direction is roughly unchanged.

Since Ti-Ti distances up to 5.43 Å are observed in the precursor, we can build a cluster (Model 1) consisting of five TiO_6 octahedra (**Fig. 3a**) that is derived from a contracted anatase structure with a unit cell of $a = 3.60$ Å and $c = 9.45$ Å to describe the short-range order of precursor structure. **Fig. 3b** is the fit of the PDF using Model 1. Because of the large disorder of O atoms in the precursor, we are unable to get a reasonable fit. If we assume the O atoms are only ordered in the closest Ti-O shell, we can model the cluster as two components where five Ti atoms are exactly the same as in Model 1 to form a framework plus one TiO_6 octahedron (**Fig. 3c**, Model 2). It can be seen in **Fig. 3d** that this simple Model 2 results in a quite good fit to the precursor but that the characteristics of the longer Ti-O distances are not described in this model. Even though the Ti-Ti distances are compressed along the *a*- and *b*-axes in the precursor structure, the length of the Ti-O bonds (corresponding to the closest Ti-O distances) should not change much compared to those in anatase TiO_2. Since most Ti-O bonds are contracted in Model 1, we further modify Model 1 by extending all the Ti-O bonds up to around 1.97 Å and keep the position of Ti atoms unchanged to make a new model (Model 3). Thus, some of the Ti atoms are in normal 6-fold coordination, but other Ti atoms only have 5-fold coordination as shown in **Fig. 3e**. Fernández-García *et al*[30] have studied the structural characteristics of the amorphous solid precursors for preparing

anatase TiO_2 by X-ray absorption structure analysis indicating that the solid precursors have similar local order as that of anatase structure but containing defective Ti atoms in 5-fold coordination in addition to normal Ti atoms with 6-fold coordination. This is in good agreement with our Model 3, and **Fig. 3f** shows a reasonable fit of the precursor PDF with this model. Note that the Ti atom at the bottom of the structure in all the above models has occupancy of about 0.4. As a result, the local structure of the amorphous precursor can be described by titanium hydroxide clusters that consist of several (4 to 5) TiO_6/TiO_5 units with an arrangement related to anatase. In all the above models the H atoms were omitted for simplification. The particle size of white suspension precursor may be much larger than a few nanometers, but there is only a small structural persistence length. In the present work, only the local-range order structure of the amorphous precursor is described, while the whole structure of the precursor could be an extended structure consisting of more clusters with different orientations. Zhang *et al*[31] synthesized solid amorphous titania composed of ~2 nm nanoparticles and PDF data was used for reverse Monte Carlo simulations of the structure of the amorphous TiO_2. It was suggested that the amorphous nanoparticles have a highly distorted shell and a strained crystalline core with an average Ti-O coordination number of 5.3. Our results show that the precursor structure in the solvent is very close to that of the solid precursor, confirming the formation of anatase TiO_2 under hydrothermal synthesis is similar to a solid state transformation.

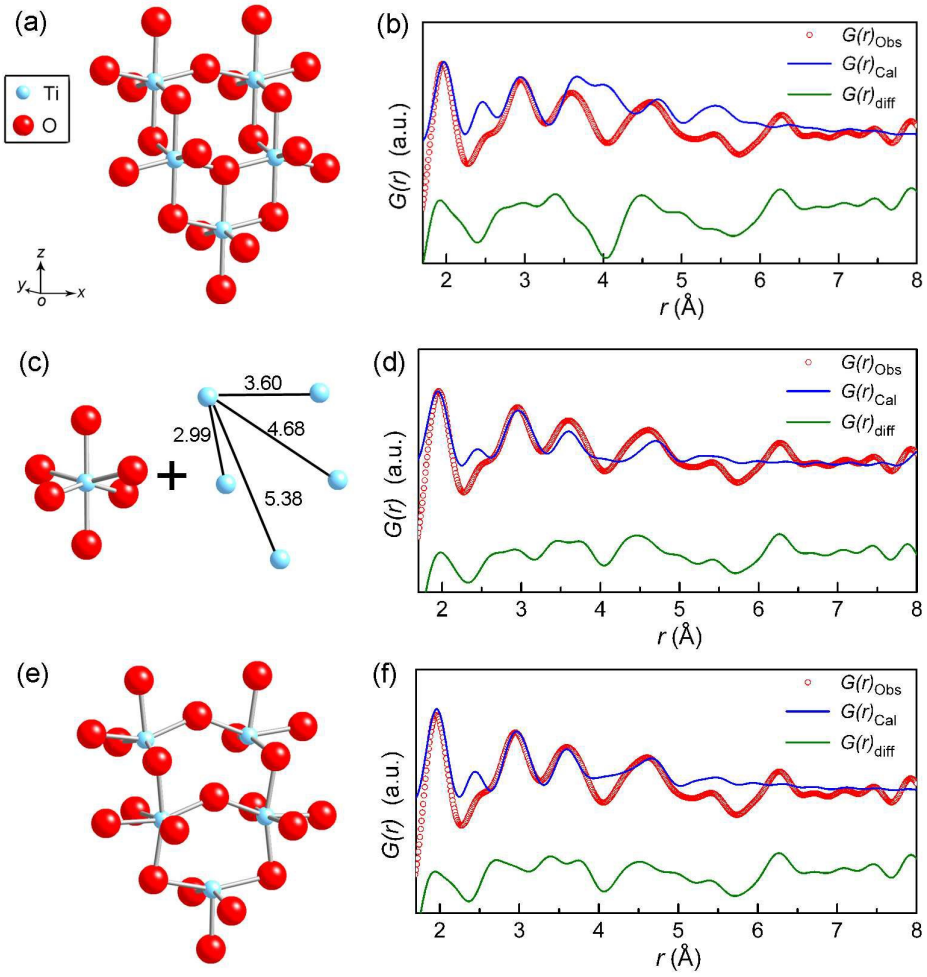

Fig. 3 Structural models and fits to the PDF *G(r)* of the precursor. The H atoms are omitted in all the models. The models only describe the local short-range order of the precursor structure. The complete structure of the white suspension precursor could be an extended network consisting of many clusters with different orientations.

Structural defects

Structural defects play a crucial role in the properties of many nanomaterials, but it is difficult to obtain direct experimental evidence of the defect type in nanoparticles. When fitting the experimental PDF at 20 minutes with the anatase structure as shown in **Fig. 2**, it is found that the model pattern agrees very well with the experimental pattern at distances above 7 Å. In contrast, the local structure ($r < 7$ Å) is not well described by the anatase structure, and this indicates that there is a large amount of defects or

disorder in the local structure of the anatase nanoparticles. Close examination of the deviations of the PDF fit shows that the intensities of the calculated peaks at 3.02 and 3.78 Å related to Ti-Ti shells are much lower than the experimental peaks, while the observed intensity of the peak at 1.97 Å from the Ti-O bonds exceeds the calculated peak (also shown in **Fig. 4a**). This indicates that the Ti atom in the nanoparticles has a lower coordination number than the ideal six-fold coordination in the bulk anatase structure. This can be understood if the product retains parts of the features of the precursor structure, i.e. that there is an amorphous part in the TiO_2 product.

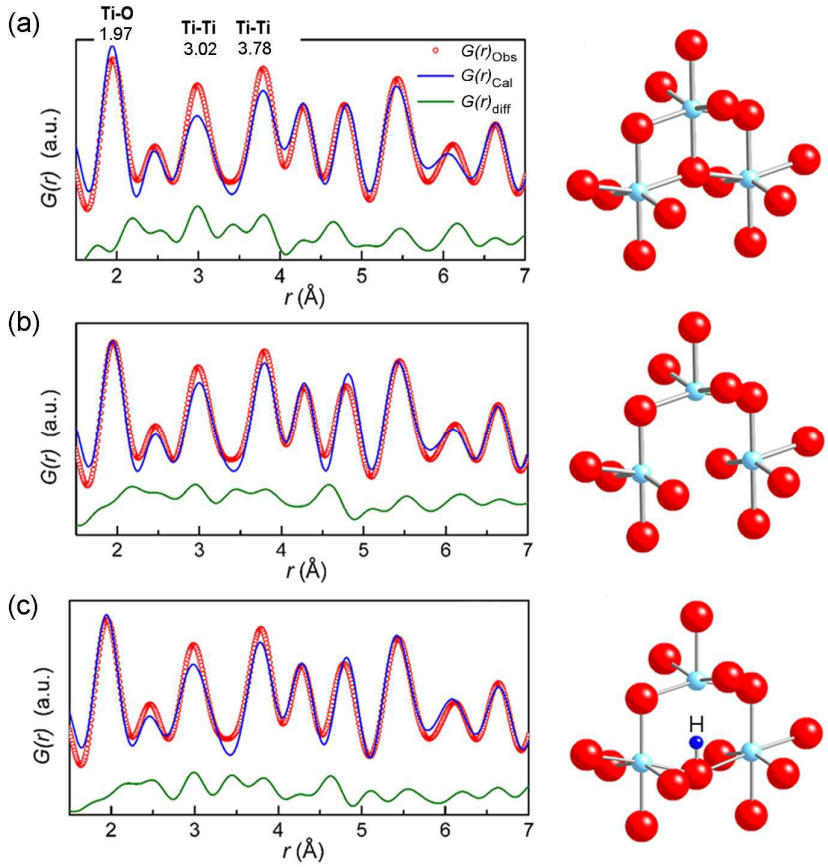

Fig. 4 Experimental, calculated and difference PDF patterns at a reaction time of 20 minutes for the short-range fits (1.5 Å < r < 7Å), (a) anatase ordered structure, R_w = 0.311, (b) anatase with oxygen vacancy, R_w = 0.270, (c) anatase with OH defects, R_w = 0.248. The refinements of the ordered structure and the oxygen vacancy structure are based on crystallographic data from the anatase TiO_2 structure, and the OH defect

model is based on a modified structure from anatase TiO_2. For clarity, only clusters are shown in the structure models to depict the different structures with or without oxygen defects.

For the analysis of the types of defect in the anatase nanoparticles, a simple, plausible explanation for the low Ti coordination number could be a large amount of oxygen vacancies. In this case, the oxygen vacancies can be implemented in the structural model by refining the oxygen occupancy without altering the local structure (see Supporting Information). Using this method, an oxygen occupancy of about 82.4% is obtained by refining the PDF in a full r range (1.5 Å < r < 60 Å). However, the refinement does not significantly improve the quality of the fit (**Fig. S2**). As shown in **Table 1**, the values of R_w are 25.2% and 25.7% for the ordered structure model and the oxygen vacancy model, respectively, which suggests that defects in the form of oxygen vacancies distributed in the crystalline lattice are unlikely. However, when the PDFs are refined only in the low r range (1.5 Å < r < 7 Å), the quality of the fit for oxygen vacancy model strongly improves compared with that of ordered structure model as shown in **Fig. 4a-b**, and R_w decreases from 31.1% for ordered structure to 27.0% for oxygen vacancy model. The oxygen occupancy for the fit of r < 7 Å is only 72.7% which is much lower than what was found from the full r range refinement. Thus, the refined oxygen occupancy is dependent on the r range fit. The refined structure is more close to an ordered structure when larger r data are included, indicating that in the large r range the disorder can be reconciled with the ordered structure. Because oxygen vacancies can not be averaged out with an ordered structure, the above analysis implies that there are other oxygen defects than oxygen vacancies in the anatase structure. The correctness of the vacancy model can be examined by analyzing the Ti content in the product nanoparticles using XRF measurement which gives a Ti weight percentage of 59.7(1) %. If we ignore any impurities in the sample, this gives $TiO_{2.02}$, i.e., stoichiometric TiO_2. This strongly suggests that the defects are not oxygen vacancies but other types of oxygen disorder.

Theoretical calculations have suggested that water dissociation on TiO_2 occurs at

the surface oxygen vacancy sites leading to the formation of two bridging hydroxyl (OH) groups.[36, 37] Actually, oxygen vacancies are hardly observed on the rutile (110) surface even in deep ultra high vacuum conditions because even a little amount of residual water molecules very quickly converts a reduced surface into a hydroxylated surface.[38] It has also been reported that bulk Ti-OH defects are quite stable and easily form in both anatase and rutile.[37] Here, we introduce the OH defects in the model as discussed in the Supporting Information. Our results suggest that OH groups which originate from the precursor structure basically replace the oxygen vacancies in TiO_2 anatase nanoparticles. **Fig. 4c** shows the PDF refinement modeled by an anatase structure with bridging hydroxyl defects for the local range of $r < 7$ Å. For this model R_w is 24.8%, which is slightly better than the vacancy model but a much better fit than the ordered structure model. In the large r range, due to the random distribution of the bridging hydroxyl defects, the disorder in OH defects model can be reconciled with the ordered structure on average.

As discussed above, the fitting pattern of ordered anatase structure agrees very well with the experiment pattern at distances above 7 Å. It is possible that the defects are only on the surface of the nanoparticles, but not really present in the bulk structure. To shed light on this, the concentrations of the oxygen defects for TiO_2 nanoparticles with different particle size are estimated. In the local r range (< 7 Å), the fits should be similar no matter if it is vacancy model or OH defects model is used since both models result in a lower coordination number of Ti atoms. Thus, a reasonable defect concentration can be estimated by refining the oxygen occupancy, where the defect concentration equals one minus the oxygen occupancy. **Fig. 5** displays the defect concentration as a function of particle size, indicating that the defect concentration decreases with increasing particle size, or increases with surface area. Based on this we suggest that the defects are mainly located at the surface of the TiO_2 nanoparticles. If we contribute the atoms at the outermost layer (with a thickness of ~ 0.2 nm) as surface atoms, the volume fraction of the surface layer of a 5 nm TiO_2 particle would be 22.2%, which is quite close to the oxygen defect concentration as shown in **Fig. 5**. The resulting TiO_2 product has a crystallinity of 76.3% as measured by PXRD using an internal

standard of CaF_2 (see the Supporting Information), and this also corroborates the surface defect model. The results agree well with the predicted model of anatase nanoparticles by molecular dynamics simulations that the surface layer appears amorphous, whereas the particle interior is the bulk anatase structure.[39]

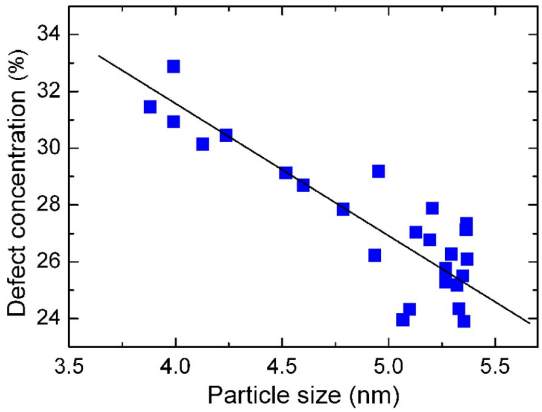

Fig. 5 Defect concentration as a function of particle size obtained by PDF analysis. The defect concentration equals one minus the oxygen occupancy.

Kinetics and crystal growth

Understanding the kinetics of crystallization and grain growth is important for obtaining controlled growth of nanoparticles with the desired properties and for understanding their thermal stability. The crystallization and grain growth for solid-state transformations have been studied in great detail.[40-42] However, the studies of kinetics under hydrothermal synthesis conditions are limited. The *in situ* total scattering method allows us to analyze the kinetics of crystallization and the crystal growth of anatase TiO_2 under hydrothermal conditions. For crystallization kinetics, solid-state phase transformation can be described using the Avrami equation:[40]

$$\alpha = 1 - \exp\left[-(k_1 t)^n\right] \quad (1)$$

where k_1 is a temperature-dependent rate constant which is related to the activation energy of the transformation, α is the fraction of transformation, t is the reaction time

and n is a parameter describing the crystallization mechanisms. Bulk nucleation mechanisms often result in n parameters larger than 1 and surface nucleation yields $n \sim 1$.[41,42] In the present study the fraction of transformation α can be estimated from the normalized scale factors (*SF*) of anatase TiO_2. **Fig. 6a** gives the time evolution of the normalized scale factors of anatase TiO_2 obtained by refinements of PDF and PXRD data respectively. Because the PDF patterns also contain the amorphous phase, the scale factors obtained by PDF are larger than those by PXRD for reaction times below 5 minutes in the initial nucleation stage. Here, we fit the time evolution of the scale factor from PXRD to the Avrami equation. A k_1 value of 1.90 min^{-1} and an n value of 0.4 are obtained with the model. Even though the formation of anatase TiO_2 under hydrothermal synthesis is likely to occur via a solid-state phase transition from amorphous titania, an n value of 0.4 is significantly smaller than 1, and it cannot be explained by any of the known bulk or surface nucleation mechanism for solid state transformations. Thus, the solvent has a large impeding effect on the crystallization kinetics under hydrothermal synthesis conditions.

Fig. 6b shows the time-dependent particle sizes obtained from the PXRD and PDF refinements. The particle size obtained from PXRD is relatively smaller because the instrumental broadening is not corrected for in the present study. A simple power law is often applied to describe the dynamics of grain growth in highly pure, coarse-grained polycrystalline materials, but this is not suitable for describing grain growth in nanocrystalline materials.[43] The presence of impurities, pores or precipitates in nanocrystalline samples gives rise to significant retarding forces (solute drag) on the grain-boundary movement. There are several models established to describe the kinetics of grain growth in nanocrystalline materials.[43,44] For the growth of anatase nanoparticles during the solid-state transitions, an empirical rate law has been used to describe the kinetics,[45]

$$D(t)^m - D_0^m = k_2 t \qquad (2)$$

where $D(t)$ and D_0 are the instantaneous and initial particle size, and m is the grain

growth exponent describing the growth mechanism. m = 2 indicates grain growth in a pure, single-phase system, and m = 3 or 4 denotes grain growth in the presence of solutes or pores. In the present case a single fit can not applied to the growth curve suggesting that there are large changes in the growth dynamics at different periods of the reaction. The "size-dependent impediment" model[44] has been reported to describe the kinetics of grain growth process of nanocrystalline materials.

$$D(t)^2 = D_{max}{}^2 - (D_{max}{}^2 - D_0{}^2)\exp[-k_3 t] \quad (3)$$

where D_{max} is the equilibrium particle size. The parameter k_3 describes the specific interface energy and grain boundary mobility, and t is the reaction time. The solid line in **Fig. 6b** is the fit of the PDF growth curve indicating that the "size-dependent impediment" model gives a reasonable description of the growth kinetics. With the known values of D_0, the resulting values of D_{max} = 5.12 nm and k_3 = 0.99 min^{-1} were obtained by fitting this model.

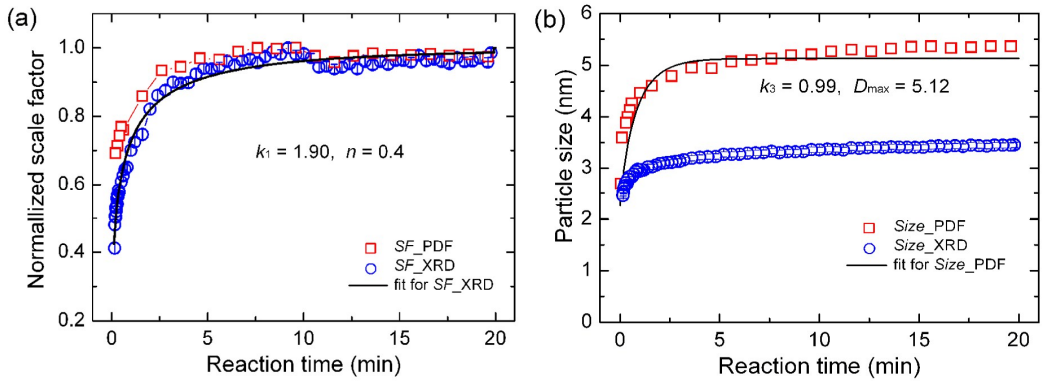

Fig. 6 (a) Time evolution of scale factors (SF) of anatase TiO_2 obtained by refinements of PDF and PXRD data respectively, the solid line is a fit using Avrami equation to the PXRD scale factors. **(b)** Grain growth curves obtained by PXRD and PDF analysis. The solid line is the fit with the "size-dependent impediment" grain-growth model to the growth curve obtained from the PDF data.

PDF versus PXRD information

It is worth mentioning the time dependence of the structure information obtained from the PXRD analysis. In **Fig. 7a** it can be seen that with increasing reaction time (increasing particle size) the cell parameter *c* increases whereas *a* remains nearly constant. Various microstrain characteristics have been reported for anatase TiO_2 nanoparticles,[39] but there is limited concrete evidence for the suggested mechanisms. In the present study, the contraction of the cell parameter *c* and the constant of cell parameter *a* with reduced particle size indicate higher microstrain in *c*-direction than in the *a*-direction, and this can be explained by the combined effects of enhanced surface stress and increased concentration of OH defects. The effect of defects on the microstrain is further implied by the change of the *z*-coordinate for the O atoms and the length of Ti-O bonds with reaction time (or particle size) as shown in **Fig. S5**. Even though the unit cell parameter *c* decreases when the particle size decreases, it is interesting to see that the length of the Ti-O bond along *c*-axis increases with reduced particle size. The bond length along *a*- or *b*-axis remains almost unchanged (data not shown).

Fig. 7b gives the time evolution of oxygen occupancies obtained from the PXRD refinements. As already discussed above for the PDF analysis, the oxygen occupancy is lower than full occupancy and decreases with reduced particle size reflecting the characteristics of the OH defects. In contrast, the oxygen occupancy obtained from PXRD is larger than full occupancy and furthermore it increases with reduced particle size. The discrepancy between the PDF and PXRD results probably is due to the fact that the PXRD analysis gives the information of a long-range average structure, whereas PDF allows extraction of structural information of the short-range local structure. In the local short-range structure, the O atoms in the OH defects are not located at the "correct" oxygen positions, and thus they can be omitted and treated identically to oxygen vacancies resulting in a low occupancy of oxygen atoms in the PDF refinement. However, the OH defects are averaged out in the long range description and thus they are part of the PXRD analysis, where the presence of H atoms artificially gives rise to a higher occupancy at the oxygen sites. Both the PXRD and the PDF results show an

increasing defect concentration with reduced particle sizes.

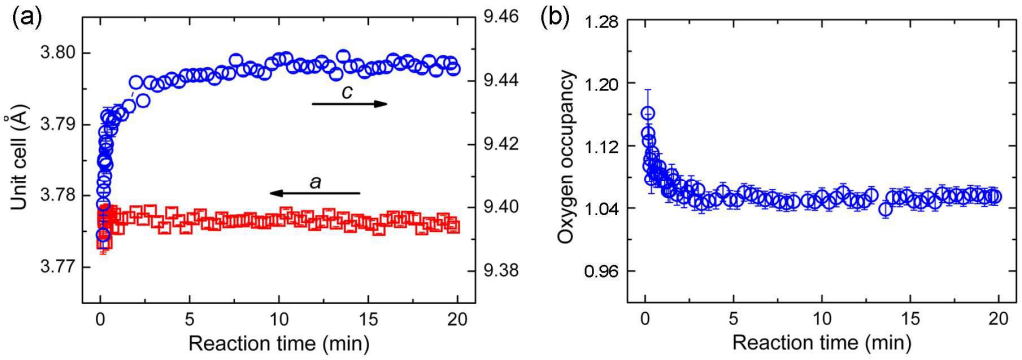

Fig. 7. Cell parameters (a) and oxygen occupancy (b) as functions of reaction time as obtained from PXRD refinements.

Experimental

The anatase TiO_2 nanoparticles were prepared by hydrothermal hydrolysis of titanium isopropoxide. The experiments were carried out at beam line ID11 at the ESRF, Grenoble, France. The experimental setup used for *in situ* studies consists of a thin, fused silica capillary heated by a flow of hot air as described in detail by Becker *et al.*[46] The precursor was made by mixing a solution of 2.0 M titanium isopropoxide $Ti(OCH(CH_3)_2)_4$ in isopropanol with an equal volume of water under stirring. This precursor was then injected into the fused silica capillary which was pressurized to 250 bar hydrostatic pressure. The reaction was initiated by applying rapid heating to 250 °C. At the same time, sequential exposure of X-ray frames with a time resolution of 1 s was started. The X-ray wavelength was λ = 0.18970 Å (65 keV), and the detector was a Frelon4M camera.

The total scattering data sets were integrated using *Fit2D*,[47] and the experimental PDF (G(*r*)) was calculated from 0 Å to 60 Å in steps of 0.01 Å using *PDFgetX3*[48] using the *Q*-range, Q_{max} = 16.8 Å^{-1} and Q_{min} = 1 Å^{-1}. The PDF data were summed to frames with a time resolution of 3 s to improve the data quality. Scattering from the capillary with deionized water at the appropriate conditions was subtracted from the integrated intensities prior to the Fourier transformation. The PDF data were modeled to extract

structural parameters and refined sequentially using *PDFgui*.[49] PXRD data with a time resolution of 1 s obtained from the total X-ray scattering data were Rietveld refined using the FullProf program[50] for the comparison of the PDF results. The resulting nanoparticles were further analyzed by X-ray fluorescence (XRF) spectroscopy on a SPECTRO XEPOS. The crystallinity was estimated by PXRD using an internal standard of CaF_2 as described in the Supporting Information and elsewhere.[51]

Conclusions

The PDF method applied to total X-ray scattering data provides detailed information about the formation and growth mechanisms as well as the structural defects of TiO_2 anatase nanoparticles. The amorphous solid precursor structure can be modeled by titanium hydroxide clusters consisting of TiO_6/TiO_5 units with an arrangement related to that of bulk crystalline anatase. Once the TiO_2 anatase nanoparticle has formed the structure contains a large amount of defects, but the data were shown not to be compatible with a structure containing oxygen vacancies. Instead the nanoparticle structure was suggested to contain OH defects in the surface layer, while the core of the particle has the bulk anatase structure. The relative number of OH defects then naturally decreases as the particle grows. The crystallization kinetics were modelled using an Avrami model and they were found to differ significantly from normal solid state phase transitions presumably due to strong solvent effects under the present hydrothermal synthesis conditions. A "size-dependent impediment" model provided a good fit to the growth curve of the nanocrystals. The information obtained separately from PDF and PXRD analysis was contrasted. Interestingly, the PXRD data indicate a larger than full oxygen occupancy for the smaller nanoparticles due to the incorrect long range description of the OH defects. Overall, the present study demonstrates the power of in situ PDF analysis for understanding the formation and growth of nanoparticles. The PDF approach can provide structural information all the way from the amorphous precursor structure over the initial highly defect pristine nanocluster to the final mature nanoparticle. Even though the present nanoparticle formation appears to be a solid state

phase transition from the amorphous precursor to the crystalline nanoparticle, the high pressure high temperature solvent conditions of the synthesis are observed to strongly affect the crystallization and growth.

Acknowledgements

The authors gratefully acknowledge the beamtime obtained at beamline ID11 at the ESRF, Grenoble, France. The work was supported by the Danish National Research Foundation (DNRF93), and DanScatt. Work at Jiangsu University was supported by the National Natural Science Foundation of China (51401089), the Natural Science Foundation of Jiangsu Province (No. BK20140552) and the Scientific Research Foundation of Jiangsu University (No. 1291220029).

References

1 A. Fujishima, T. N. Rao and D. A. Tryk, *J. Photochem. Photobiol. C: Photochem. Rev.*, 2000, **1**, 1-21.

2 A. Fujishima and K. Honda, *Nature*, 1972, **238**, 37-38.

3 B. O'Regan and M. Grätzel, *Nature*, 1991, **353**, 737-740.

4 Z. Zou, J. Ye, K. Sayama and H. Aralawa, *Nature*, 2001, **414**, 625-627.

5 Y. Fan, G. Chen, D. Li, Y. Luo, N. Lock, A. P. Jensen, A. Mamakhel, J. Mi, S. B. Iversen, Q. Meng and B. B. Iversen, *Int. J. Photoenergy*, 2012, **2012**, 173865.

6 J. M. Pettibone, D. M. Cwiertny, M. Scherer and V. H. Grassian, *Langmuir*, 2008, **24**, 6659-6667.

7 N. Pienack and W. Bensch, *Angew. Chem. Int. Ed.*, 2011, **50**, 2014-2034.

8 S. J. L. Billinge and I. Levin, *Science*, 2007, **316**, 561-565.

9 J. L. Mi, M. Christensen, C. Tyrsted, K. Ø. Jensen, J. Becker, P. Hald and B. B. Iversen, *J. Phys. Chem. C*, 2010, **114**, 12133-12138.

10 J. L. Mi, T. N. Jensen, M. Christensen, C. Tyrsted, J. E. Jørgensen and B. B. Iversen, *Chem. Mater.*, 2011, **23**, 1158-1165.

11 N. Lock, M. Christensen, K. M. Ø. Jensen and B. B. Iversen, *Angew. Chem. Int. Ed.*, 2011, **50**,

7045-7047.

12 J. L. Mi, Y. B. Shen, J. Becker, M. Bremholm and B. B. Iversen, *J. Phys. Chem. C*, 2014, **118**, 11104-11110.

13 M. Bremholm, J. Becker-Christensen and B. B. Iversen, *Adv. Mater.*, 2009, **21**, 3572-3575.

14 F. Xia, D. Chen, N. V. Y. Scarlett, I. C. Madsen, D. Lau, M. Leoni, J. Ilavsky, H. E. A. Brand and R. A. Caruso, *Chem. Mater.*, 2014, **26**, 4563-4571.

15 H. Jensen, M. Bremholm, R. P. Nielsen, K. D. Joensen, J. S. Pedersen, H. Birkedal, Y. S. Chen, J. Almer, E. G. Søgaard, S. B. Iversen and B. B. Iversen, *Angew. Chem. Int. Ed.*, 2007, **46**, 1113-1116.

16 G. V. Jensen, M. Bremholm, N. Lock, G. R. Deen, T. R. Jensen, B. B. Iversen, M. Niederberger, J. S. Pedersen and H. Birkedal, *Chem. Mater.*, 2010, **22**, 6044-6055.

17 J. R. Eltzholtz, C. Tyrsted, K. M. Ø. Jensen, M. Bremholm, M. Christensen, J. Becker-Christensen and B. B. Iversen, *Nanoscale*, 2013, **5**, 2372-2378.

18 J. L. Mi, C. Clausen, M. Bremholm, N. Lock, K. M. Ø. Jensen, M. Christensen and B. B. Iversen, *Cryst. Growth Des.*, 2012, **12**, 6092-6097.

19 T. Proffen and H. Kim, *J. Mater. Chem.*, 2009, **19**, 5078-5088.

20 C. A. Young and A. L. Goodwin, *J. Mater. Chem.* 2011, **21**, 6464-6476.

21 S. J. L. Billinge and M. G. Kanatzidis, *Chem. Commun.*, 2004, 749-760.

22 M. A. Newton, K. W. Chapman, D. Thompsett and P. J. Chupas, *J. Am. Chem. Soc.*, 2012, **134**, 5036-5039.

23 G. Paglia, E. S. Bozin and S. J. L. Billinge, *Chem. Mater.*, 2006, **18**, 3242-3248.

24 P. J. Chupas, K. W. Chapman, H. L. Chen and C. P. Grey, *Catal. Today*, 2009, **145**, 213-219.

25 K. M. Ø., Jensen, C. Tyrsted, M. Bremholm and B. B. Iversen, *CHEMSUSCHEM*, 2014, **7**, 1594-1611.

26 D. Saha, K. M. Ø. Jensen, C. Tyrsted, E. D. Bøjesen, A. H. Mamakhel, A. C. Dippel, M. Christensen and B. B. Iversen, *Angew. Chem. Int. Ed.*, 2014, **53**, 3667-3670.

27 C. Tyrsted, K. M. Ø. Jensen, E. D. Bøjesen, N. Lock, M. Christensen, S. J. L. Billinge and B. B. Iversen, *Angew. Chem. Int. Ed.*, 2012, **51**, 9030-9033.

28 K. M. Ø. Jensen, M. Christensen, P. Juhas, C. Tyrsted, E. D. Bøjesen, N. Lock, S. J. L. Billinge and B. B. Iversen, *J. Am. Chem. Soc.* 2012, **134**, 6785-6792.

29 C. Tyrsted, N. Lock, K. M. Ø. Jensen, M. Christensen, E. D. Bøjesen, H. Emerich, G. Vaughan, S. J. L. Billinge and B. B. Iversen,. *IUCrJ*, 2014, **1**, 165-171.

30 M. Fernández-García, C. Belver, J. C. Hanson, X. Wang and J. A. Rodriguez, *J. Am. Chem. Soc.*, 2007, **129**, 13604-13612.

31 H. Zhang, B. Chen and J. F. Banfield, *Phys. Rev. B*, 2008, **78**, 214106.

32 O. Bikondoa, C. L. Pang, R. Ithnin, C. A. Muryn, H. ONishi and G. Thornton, *Nat. Mater.*, 2006, **5**, 189-192.

33 I. E. Grey and N. C. Wilson, *J. Solid State Chem.*, 2007, **180**, 670-678.

34 H. Kaftelen, K. Ocakoglu, R. Thomann, S. Tu, S. Weber and E. Erdem, *Phys. Rev. B*, 2012, **86**, 014113.

35 E. Erdem, *J. Alloys Compd.*, 2014, **605**, 34-44.

36 A. Tilocca and A. Selloni, *J. Phys. Chem. B*, 2004, **108**, 4743-4751.

37 A. A. Bonapasta, F. Filippone, G. Mattioli and P. Alippi, *Catal. Today*, 2009, **144**, 177-182.

38 S. Wendt, R. Schaub, J. Matthiesen, E. K. Vestergaard, E. Wahlström, M. D. Rasmussen, P. Thostrup, L. M. Molina, E. Lægsgaard, I. Stensgaard, B. Hammer and F. Besenbacher, *Surf. Sci.*, 2005, **598**, 226-245.

39 H. Zhang and J. F. Banfield, *Chem. Rev.*, 2014, **114**, 9613-9644.

40 H. Zhang and J. F. Banfield, *Chem. Mater.*, 2002, **14**, 4145-4154.

41 K. Matusita and S. Sakka, *J. Non-Cryst. Solids*, 1980, **38**, 741-746.

42 M. Fernández-García, X. Wang, C. Belver, J. C. Hanson and J. A. Rodriguez, *J. Phys. Chem. C*, 2007, **111**, 674-682.

43 A. Michels, C. E. Krill, H. Ehrhardt, R. Birringer and D. T. Wu, *Acta Mater.*, 1999, **47**, 2143-2152.

44 H. Natter, M. Schmelzer, M. S. Lőffler, C. E. Krill, A. Fitch and R. Hempelmann, *J. Phys. Chem. B*, 2000, **104**, 2467-2476.

45 B. L. Kirsch, E. K. Richman, A. E. Riley and S. H. Tolbert, *J. Phys. Chem. B*, 2004, **108**, 12698-12706.

46 J. Becker, M. Bremholm, C. Tyrsted, B. Pauw, K. M. Ø. Jensen, J. Eltzholtz, M. Christensen and B. B. Iversen, *J. Appl. Crystallogr.*, 2010, **43**, 729-736.

47 A. P. Hammersley, S. O. Svensson, M. Hanfland, A. N. Fitch and D. Hausermann, *High*

Pressure Res., 1996, **14**, 235-248.

48 P. Juhas, T. Davis, C. L. Farrow and S. J. L. Billinge, *J. Appl. Crystallogr.*, 2013, **46**, 560-566.

49 C. L. Farrow, P. Juhas, J. W. Liu, D. Bryndin, E. S. Bozin, J. Bloch, T. Proffen and S. J. L. Billinge, *J. Phys.: Condens. Matter*, 2007, **19**, 335219.

50 J. Rodriguez-Carvajal, *Physica B*, 1993, **192**, 55-69.

51 J. L. Mi, S. Johnsen, C. Clausen, P. Hald, N. Lock, L. Sø and B. B. Iversen, *J. Mater. Res.*, 2012, **28**, 333-339.

Table of Contents

The *in situ* PDF method provides detailed information about the formation and growth mechanisms of TiO_2 anatase nanoparticles under hydrothermal conditions.